# Fourier-domain imaging condition for shot-profile migration

*Brad Artman and Sergey Fomel*[1]

## ABSTRACT

Cross-correlating up-coming and down-going wavefields inherently applies a spatial multiplication. This multiplication could be performed in the wave-number domain as a convolution. However, the full imaging condition, including subsurface offset, transforms to a Fourier domain equivalent that is also a lagged multiplication. This fact allows for the simple analysis of anti-aliasing criteria. Migrations with synthetic data with flat and dipping reflectors in a homogeneous medium are produced to evaluate the Fourier domain algorithm and shots from the Marmousi data set are shown as examples of its efficacy. Periodic replications in the image space are introduced when solving the imaging condition in the Fourier domain which make results unsatisfactory. The cost of computing the imaging condition in the Fourier domain is much higher than its space domain equivalent since very few subsurface offsets need to be imaged if the velocity model is reasonably accurate. Analysis of the Fourier domain imaging condition leads to the conclusion that anti-aliasing efforts can be implemented post-migration.

## INTRODUCTION

Artman et al. (2003) introduced the advantages of a Fourier domain imaging condition for shot-profile migration in order to address aliasing problems due to unequal discretization of source and receiver acquisition geometries. It was posited, though not rigorously proven, that the details of the obvious implementation were also a lagged multiplication of the wavefields in the Fourier-domain.

When subsurface offset is introduced to the space-domain imaging condition, it is not a strict multiplication across the space axis. The lagged multiplication of the up- and down-going wavefields exist somewhere between simple multiplication and cross-correlation. By summing over the offset axis we are generating, we would be performing a rigorous correlation in space. Maintaining this axis invalidates the conventional relationships of operations in dual spaces that, in this case, results in symmetric (though not perfectly), imaging conditions in both the space and Fourier-domains.

In the theory below, we develop the imaging condition in terms of $k_x$ and $k_h$. We then present synthetic migrations with the Fourier-domain imaging condition to show its equivalence with the space-domain imaging condition. There are, however, several key differences,

---

[1]**email:** brad@sep.stanford.edu, sergey.fomel@beg.utexas.edu

associated with aliased replications, between the two results that can be seen by viewing the results in the $x - h$ plane at the depth of an imaging point. These have important ramifications for the use of this form of the imaging condition at shallow depths. Finally, by inspecting the form of the equation, we can see how the implementation of anti-aliasing criteria can be appropriately applied post-migration. This happy fact is beneficial because the Fourier-domain imaging condition is much more expensive to calculate than its space-domain equivalent.

## THEORY

The space-domain shot-profile imaging condition including subsurface offset for shot-profile migration (Rickett and Sava, 2002) is

$$I(x,h)|_{\omega,z} = U(x+h) D^*(x-h), \tag{1}$$

Where $I$ is the migrated image produced by cross-correlating the up-coming, $U$, and down-going, $D$, wavefields at every depth and frequency. Both $x$ and $h$ can be areal vectors. $*$ represents complex conjugation. To derive the Fourier-domain equivalent, we will perform a piece-wise proof and begin with the Fourier transform $D^*$ to $\hat{D}^*$ (neglecting Fourier scaling)

$$\hat{I}(x,h) = U(x+h) \int \hat{D}^*(k_s) e^{i k_s (x-h)} dk_s . \tag{2}$$

Continue by Fourier transforming the variable $x$ to find

$$\hat{I}(k_x,h) = \int U(x+h) \int \hat{D}^*(k_s) e^{i k_s (x-h)} dk_s e^{-i x k_x} dx . \tag{3}$$

By reordering variables, the equivalent form

$$
\begin{aligned}
\hat{I}(k_x,h) &= \int \hat{D}^*(k_s) e^{-i k_s h} \int U(x-h) e^{-i x (k_x-k_s)} dx \, dk_s \\
&= \int \hat{D}^*(k_s) e^{i h (k_x-2k_s)} \int U(x') e^{-i x' (k_x-k_s)} dx' \, dk_s
\end{aligned}
\tag{4}
$$

is achieved. From here, we can recognize the inner integral is the Fourier transform of the wavefield $U$ which can be replaced directly to yield

$$\hat{I}(k_x,h) = \int \hat{U}(k_x - k_s) \hat{D}^*(k_s) e^{i h (k_x-2k_s)} dk_s . \tag{5}$$

With the use of the definition of offset, $k_h = k_x - 2k_s$, we can replace several of the above arguments with equivalent expressions to find

$$\hat{I}(k_x,h) = \frac{1}{2} \int \hat{U}\left(\frac{k_x+k_h}{2}\right) \hat{D}^*\left(\frac{k_x-k_h}{2}\right) e^{i h k_h} dk_h . \tag{6}$$

The last integral is recognized as an inverse Fourier transform, this time over the $k_h$ variable. Using this fact, we arrive at the multi-dimensional (over $x$ and $h$, which can be two-dimensional themselves) Fourier transform of the general shot-profile imaging condition

$$\widehat{I}(k_x,k_h) = \frac{1}{2} \hat{U}\left(\frac{k_x+k_h}{2}\right) \hat{D}^*\left(\frac{k_x-k_h}{2}\right) . \tag{7}$$

From this equation, the result that the Fourier-domain equivalent to the conventional space-domain imaging condition for shot-profile migration is again a lagged multiplication of the up-coming and down-going wavefields at each frequency and depth level. Evaluating the arguments inside the wavefields to produce a component of the image shows that the wavefields, in the wavenumber domain, will need to be interpolated by a factor of two to calculate the image space output. The Table 1 showing example calculations of the components of the image space looks like

$$k_h$$

|        | $-1$ | $0$ | $1$ |
|--------|------|-----|-----|
| $-1$ | $\hat{U}(\frac{-2}{2})\hat{D}^*(0)$ | $\hat{U}(\frac{-1}{2})\hat{D}^*(\frac{-1}{2})$ | $\hat{U}(0)\hat{D}^*(\frac{-2}{2})$ |
| $0$ | $\hat{U}(\frac{-1}{2})\hat{D}^*(\frac{1}{2})$ | $\hat{U}(0)\hat{D}^*(0)$ | $\hat{U}(\frac{1}{2})\hat{D}^*(\frac{-1}{2})$ |
| $1$ | $\hat{U}(0)\hat{D}^*(\frac{2}{2})$ | $\hat{U}(\frac{1}{2})\hat{D}^*(\frac{1}{2})$ | $\hat{U}(\frac{2}{2})\hat{D}^*(0)$ |
| $2$ | $\hat{U}(\frac{1}{2})\hat{D}^*(\frac{3}{2})$ | $\hat{U}(\frac{2}{2})\hat{D}^*(\frac{2}{2})$ | $\hat{U}(\frac{3}{2})\hat{D}^*(\frac{1}{2})$ |

($k_x$ labels the rows.)

Table 1: Layout of wavenumber components in Fourier-domain imaging conditions

## SYNTHETIC TESTS

To test the above algorithm, synthetic data was generated and migrated with both the conventional space-domain and Fourier-domain imaging conditions. Images were created by migrating a single shot produced over a single reflecting layer within a constant velocity medium. The location, $x$, and offset, $h$, axes had the same extent and sampling. This is true for both implementations of the imaging condition.

Figure 1 shows the comparison of the space-domain impulse response to the Fourier equivalent developed above for the zero dip reflector. Both seem to provide identical results when viewed at subsurface offset $h = 0$ at the $x - z$ plane. The smile shapes are due to the limited extent of the acquisition along the surface. However, Figure 2 compares the algorithms across the $x - h$ plane at the depth of a correctly migrated image point. While at zero offset the two images are the same, the Fourier-domain implementation has obvious replications at the end of the dog-bone shaped energy distribution. Aliased energy is also introduced into the upper-right and lower-left corners of the image space. This periodicity is not encountered with the space-domain implementation.

By adding dip to the reflection point, the dog-bone shape in the $x - h$ plane becomes skewed. Figures 3 and 4 are produced with a reflector with $20^o$ and $40^o$ dip respectively. While the zero-offset image of the $x - z$ plane remains the same, the periodicity of the Fourier-
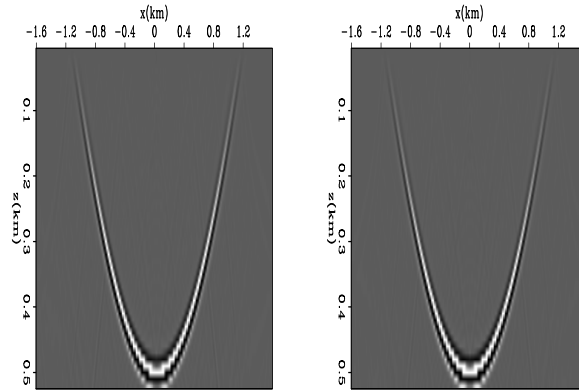
Figure 1: Migration impulse response through a constant velocity medium of both space-domain and Fourier domain implementation of the shot-profile imaging condition viewed at $h = 0$ on the $x - z$ image plane. brad3-imp [CR]

Figure 2: Migration impulse response through a constant velocity medium of both space-domain and Fourier domain implementation of the shot-profile imaging condition viewed at the depth of a focused image point on the $x - h$ image plane. brad3-imp-comp [CR]
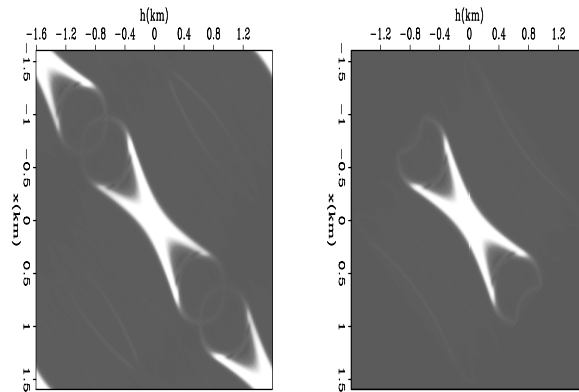
domain algorithm is again visible as compared to the computation of the imaging condition in the space-domain. Notice that as dip increases, the saddle point of the dog-bone has moved away from zero offset and the image gives the sense of tipping into the page.

Figure 3: $20^o$ dip reflector image comparison. Left is Fourier-domain implementation. Right is space-domain implementation. Image is extracted at the depth of a focused image point on the $x - h$ image plane. brad3-imp-dip-comp [CR]
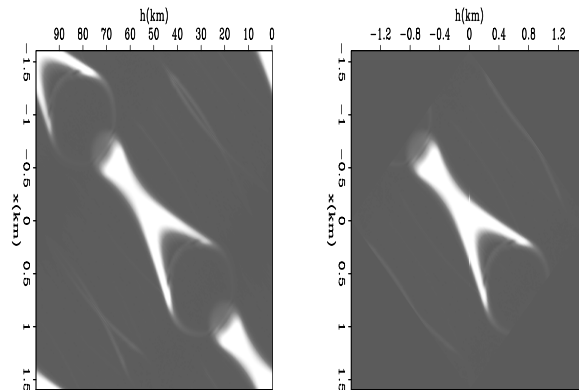
The onset of the replications are at precisely half the offset and surface location axes. To remove this type of artifact in the Fourier domain, interpolation of both axes by a factor of two would be required. From equation 7, we note that the wavefields have already required a factor of two interpolation to facilitate the algorithm. Interpolating the image by a factor of two again substantially increases memory consumption and computational effort for this implementation.

The first shot from the Marmousi synthetic data was migrated to examine the effects of the

Figure 4: 40° dip reflector image comparison. Left is Fourier-domain implementation. Right is space-domain implementation. Image is extracted at the depth of a focused image point on the $x - h$ image plane. brad3-imp-dip-2-comp [CR]
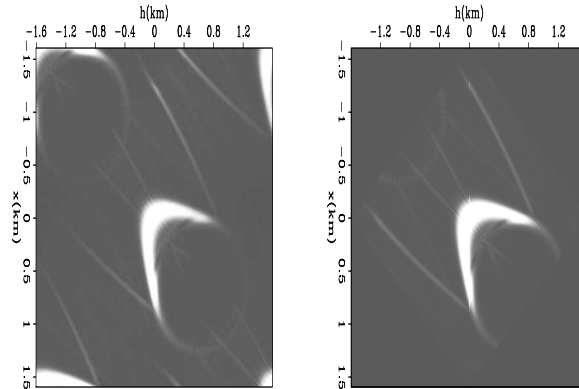
above periodicity injected into the image using the Fourier-domain imaging condition. Figure 5 compares the image from the first shot in the data computed with both space-domain and Fourier-domain imaging conditions. At great depth, the images are largely comparable, while at less than 1000 meters, the images are completely different. This is due to the combined effects of periodicity of the Fourier computed image and the steep dips of the model.

Figure 5: Images from the first shot in the Marmousi data set. Left panel computed with the Fourier-domain imaging condition, and the right panel with the conventional space domain algorithm. brad3-marm.new [CR]
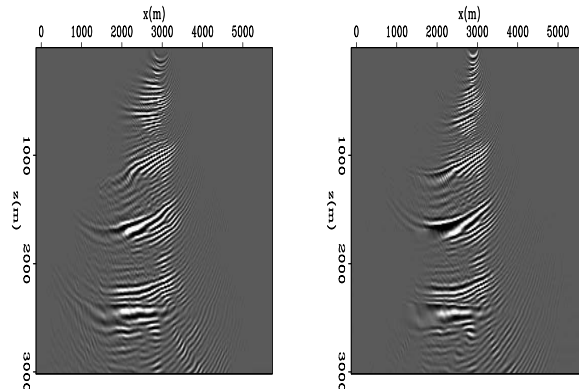
Deeper in the section, the problem is less apparent and the Fourier domain imaging condition is much closer to the space-domain result. Figure 6 demonstrates how the zeroing of the evanescent waves through the course of the migration effectively limits the range of wavenumber energy allowed into the image. After the evanescent limitations are more restrictive than the effects of the Fourier domain periodicity, the artifacts begin to diminish.

However, the images for a complex medium are definitely not strictly equivalent for the two alternative imaging condition implementations. By interpolating the $k_x$ and $k_h$ axes, it is possible to remove the limitation imposed by the periodicity at the memory/disk cost of $4n_x^2$ per depth level.

## ANTI-ALIASING IMPLICATIONS

Figure 7 shows the impact on the image space of subsampling the shot axis by a factor of ten while migrating the flat reflector synthetic data described above. The left panel imaged with

Figure 6: Images from the first shot in the Marmousi data set. Depth slices, computed with the Fourier domain imaging condition, are extracted from $z = 250$m and z=1188m. brad3-dslice [CR]
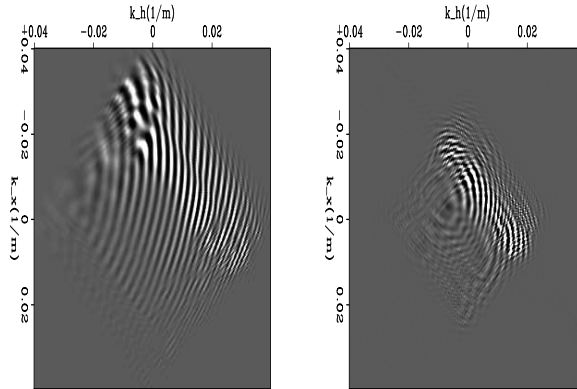
only every tenth shot, while right panel migrated shots at every receiver location. The shot-axis, which could be drawn at a $45^o$ angle up and to the right, shows inappropriate replications (Rickett and Sava, 2002). The data are modeled with sufficient receiver density, that this level of decimation does not alias the receiver gathers. This is corroborated by the absence of aliased energy in the upper-left and lower right quadrants.



Figure 7: Left panel shows the wavenumber energy for a migrated flat reflector when using sources at every tenth receiver location. On the left, and all source locations. brad3-alias-flat [CR]
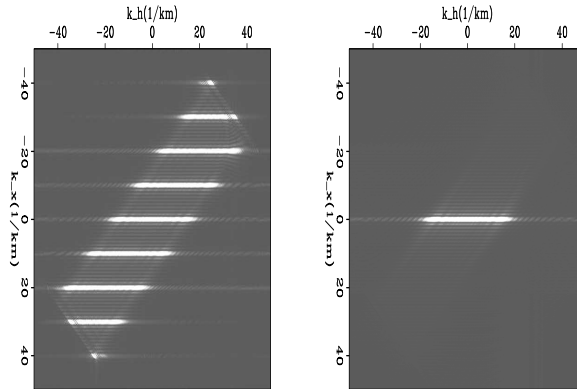
From this simple example, we can see that the anti-aliasing restriction required for the decimated migration are sloped lines to remove energy from the upper-right and lower-left quadrants. In general, any of the four corners may experience aliased replications depending on the inequality between receiver and source sampling during acquisition. The form of the imaging condition in the Fourier domain as shown in equation 7 provides important insight into how to implement anti-aliasing criteria for shot-profile migration.

Limiting the image by neither constant $k_x$ nor $k_h$ will appropriately remove the aliased energy of Figure 7. Instead, one should limit the maximum bandwidth of both the $\hat{U}$ and $\hat{D}^*$ wavefields. Table 1 provides a convenient display of this fact. This will maintain the center diamond of appropriate energy. If the anti-aliasing bandlimit is applied to the image space instead of the two wavefields used to calculate it, there are two important conclusions: 1) the bandlimit should be the same for both the offset and location axes, and 2) the limit is a diamond shaped, not circular, filter on the $k_x - k_h$ plane.

# CONCLUSION

The calculation of subsurface offset in the conventional space-domain imaging condition condition for shot-profile migration requires a series of lagged multiplications of the up-coming and down-going wavefields. Because it is not a simple multiplication, the development of its Fourier is required rather than axiomatically assuming it to take the form of a convolution. The result shown above has a very similar lagged multiplication form to its space-domain equivalent.

Several interpolations are required to implement the imaging condition as a function of wave number. First, the input wavefields, and then the calculated model space, must be twice finer sampled in wavenumber. Completely inadequate results are obtained for complex earth models if both interpolation steps are not honored. These steps increase the memory and computational demands of the method to unacceptable levels. Further, an equal number of offset-wavenumbers must be calculated to avoid aliasing as opposed to $O(10)$ for a space-domain implementation where one is reasonably confident in the accuracy of the velocity model.

Analyzing the form of the imaging condition allows us to make important conclusions about how to mitigate migration aliasing problems inherent with shot-profile migrations when the source and receiver sampling is unequal. Most importantly, anti-aliasing strategies can be implemented in the image domain after migration without needing to resort to the very expensive Fourier-domain imaging condition.

While the development of a Fourier-domain imaging condition for shot-profile migration has been presented, the periodicity of the process introduces unwanted artifacts into the image result. The form of the equation, however, provides rigor and understanding as to how to design anti-aliasing filters for data sets that do not have equal sampling of the source and receiver data axes. Further, these bandlimits can be applied on smaller post-migration volumes, possibly even during the course of converting subsurface offset to angle in the Fourier-domain at little to no additional cost.

# REFERENCES

Artman, B., Biondi, B., and Shragge, J., 2003, Operator aliasing in wavefield continuation migration: Soc. of Expl. Geophys., 73rd Ann. Internat. Mtg., 1091–1093.

Rickett, J. E., and Sava, P. C., 2002, Offset and angle-domain common image-point gathers for shot-profile migration: Geophysics, **67**, no. 03, 883–889.